Electronic Supplementary Material (ESI) for Polymer Chemistry.

Supporting Information

Design and Characterization of Ultrastable, Biopassive and Lubricious Cyclic Poly(2-alkyl-2-oxazoline) Brushes

Wenqing Yan, Mohammad Divandari, Jan-Georg Rosenboom, Shivaprakash N. Ramakrishna, Lucca Trachsel, Nicholas D. Spencer, Giulia Morgese, Edmondo M. Benetti

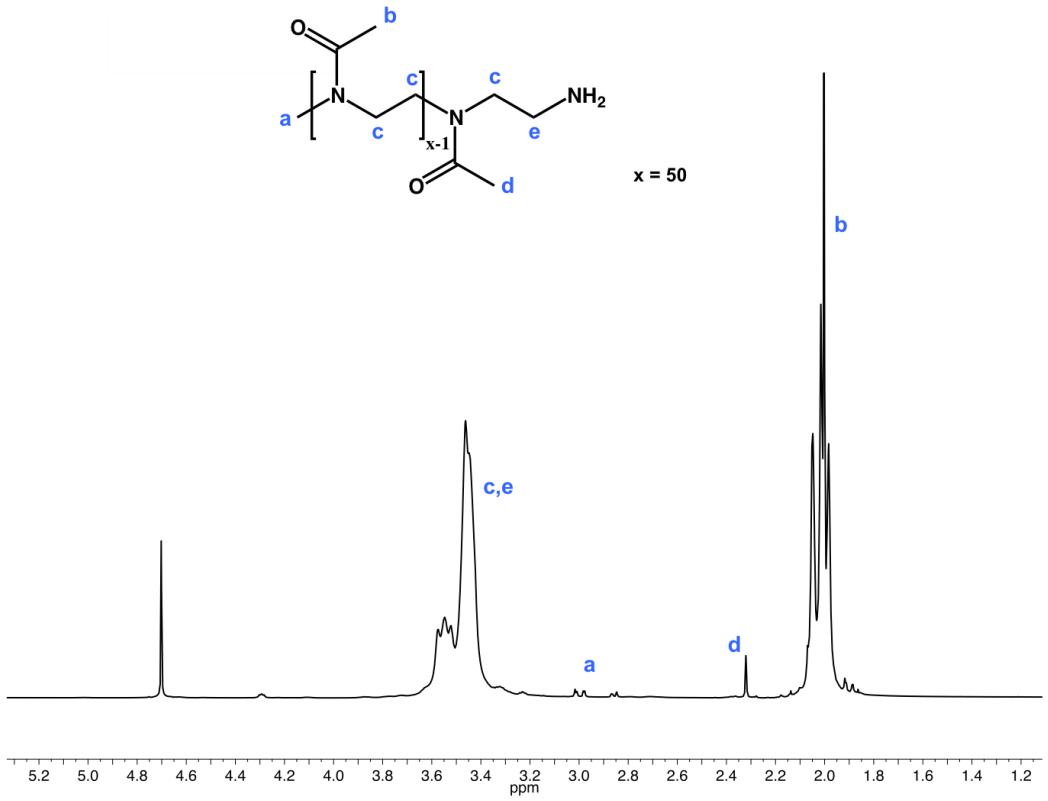

Figure S1. ^{1}H-NMR spectrum (500 MHz) of l-PMOXA in D_2O.

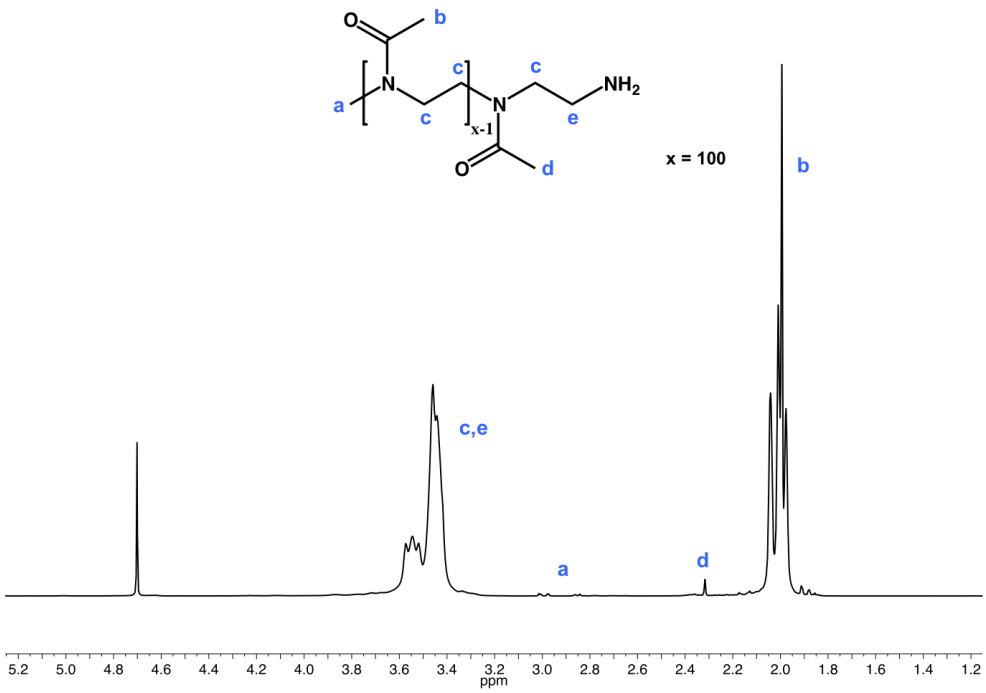

Figure S2. ^{1}H-NMR spectrum (500 MHz) of L-PMOXA in D_2O.

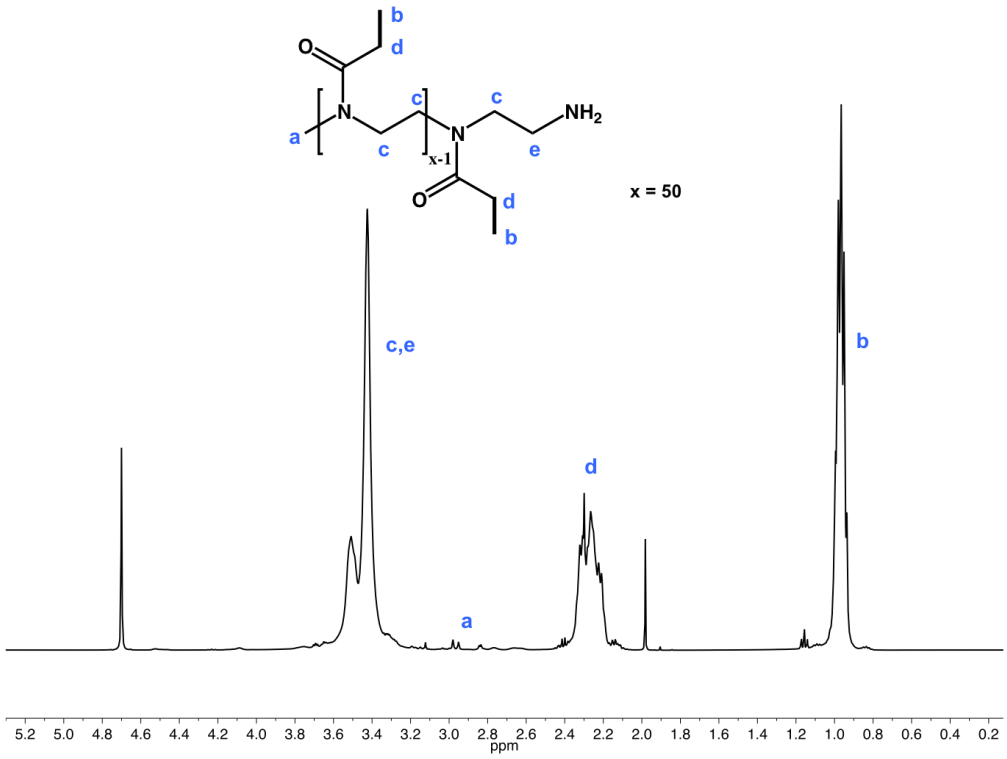

Figure S3. ^{1}H-NMR spectrum (500 MHz) of l-PEOXA in D_2O.

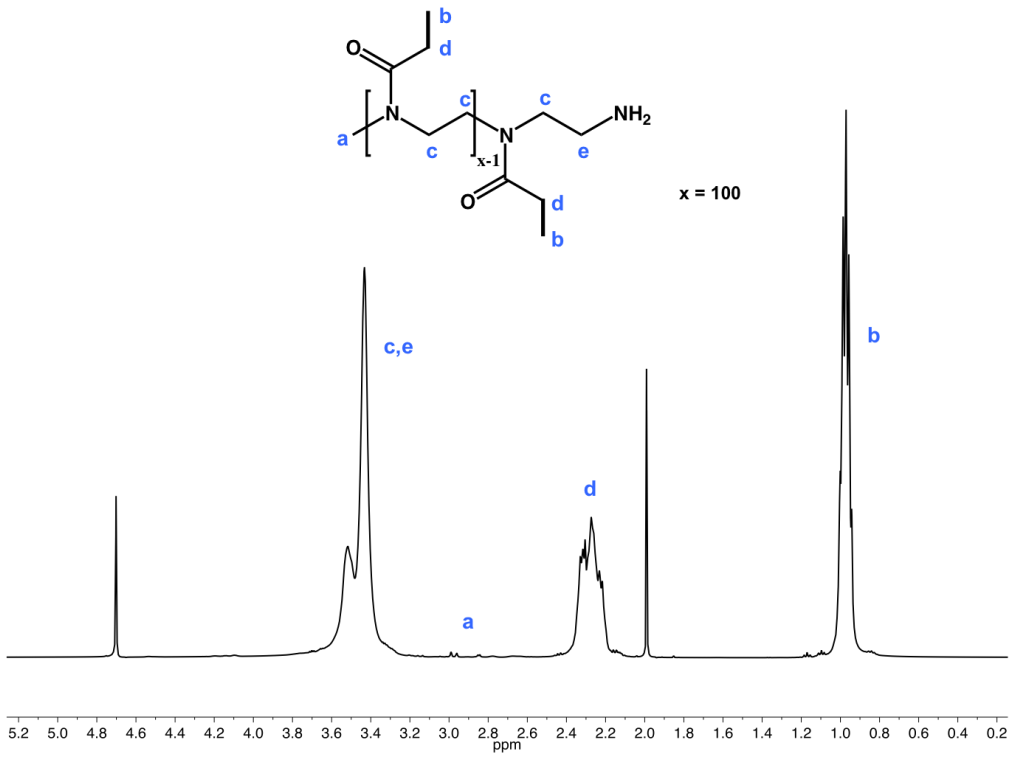

Figure S4. ^{1}H-NMR spectrum (500 MHz) of L-PEOXA in D_2O.

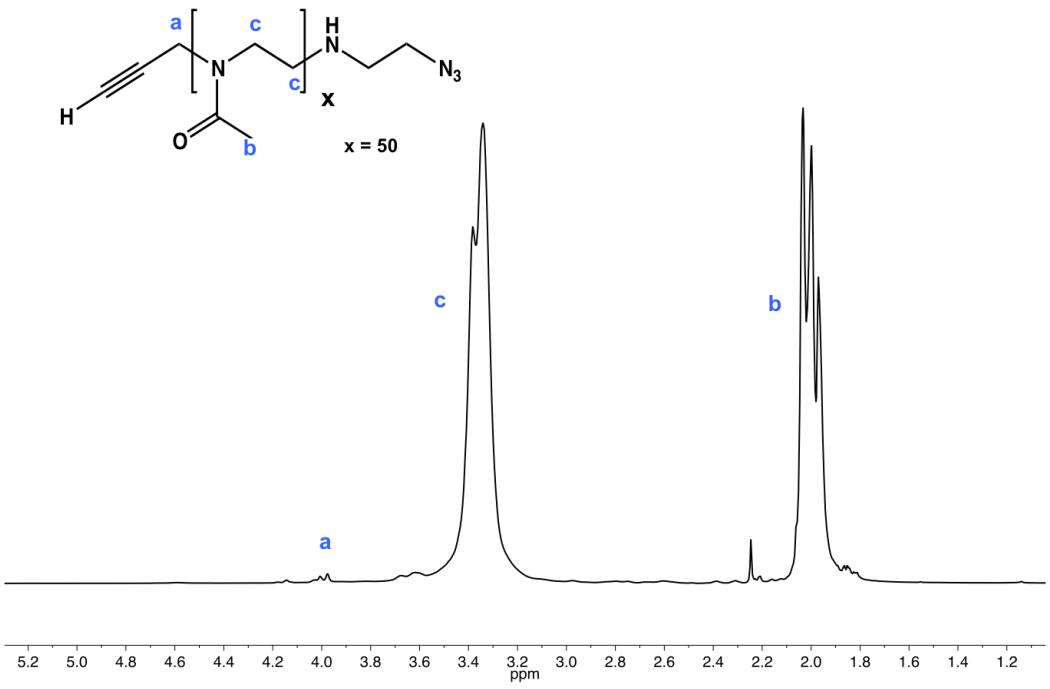

Figure S5. ^{1}H-NMR spectrum (500 MHz) of propargyl-l-PMOXA-azide in $CDCl_3$.

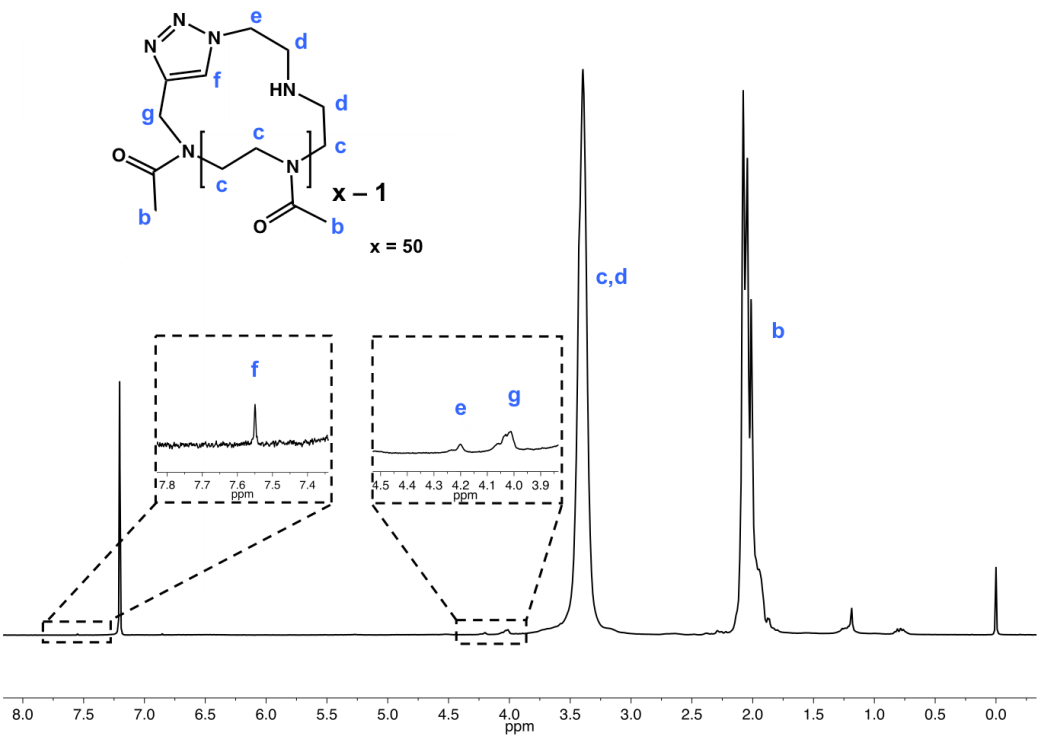

Figure S6. ^{1}H-NMR spectrum (500 MHz) of c-PMOXA in $CDCl_3$.

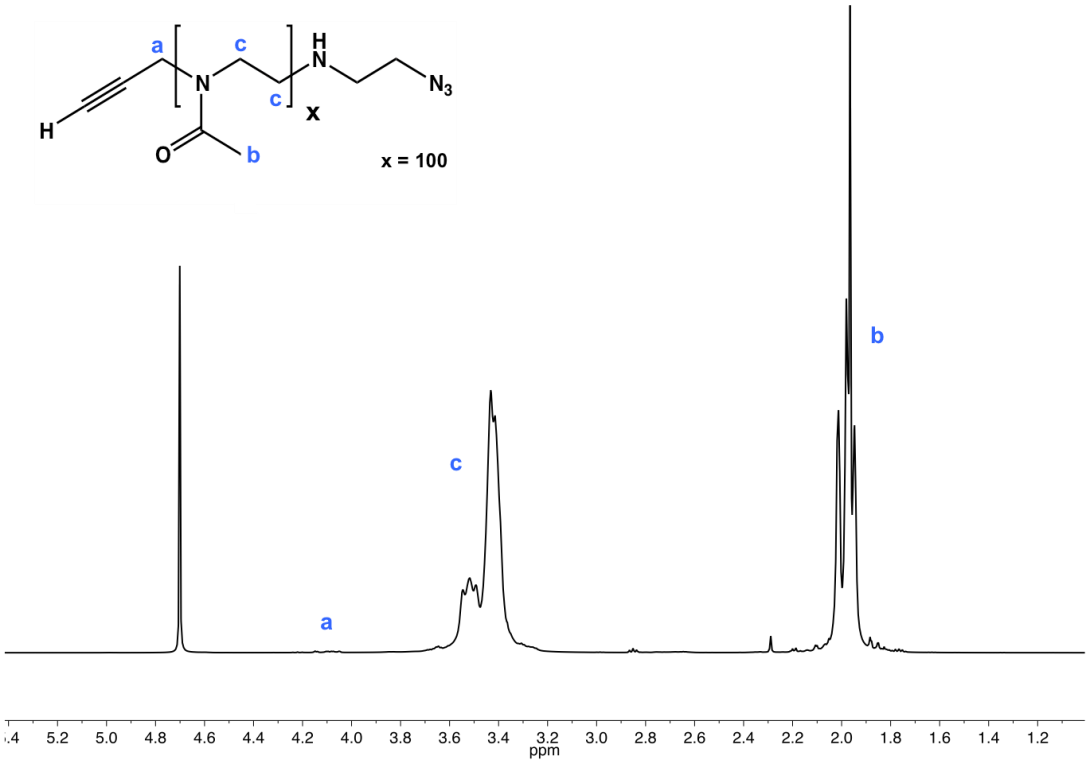

Figure S7. ^{1}H-NMR spectrum (500 MHz) of propargyl-L-PMOXA-azide in D_2O.

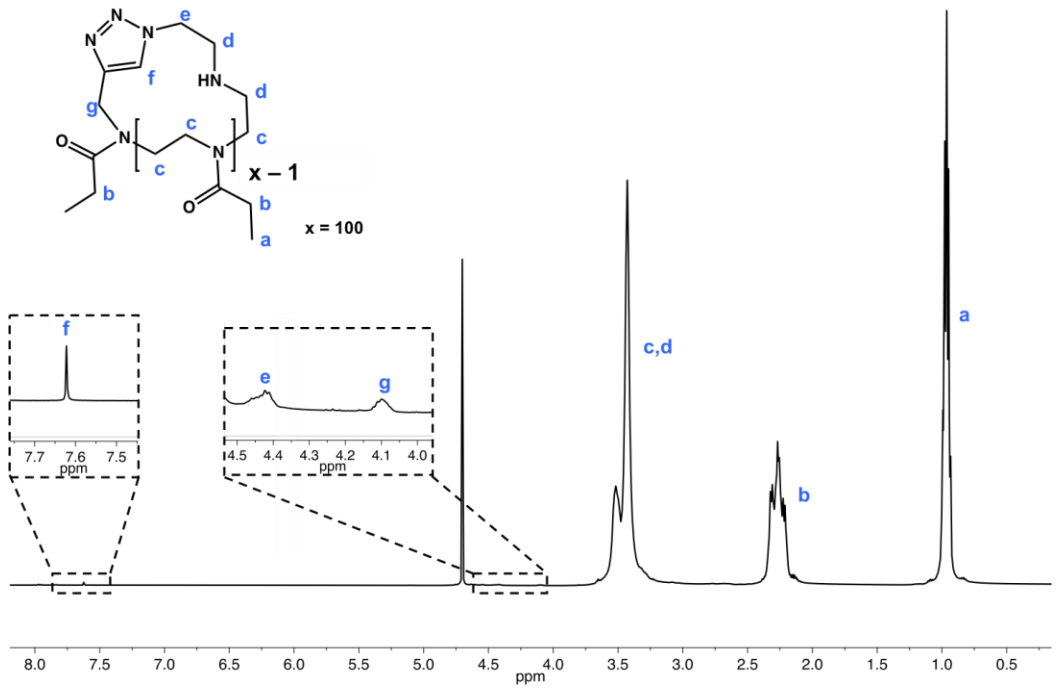

Figure S8. ^{1}H-NMR spectrum (500 MHz) of C-PMOXA in D_2O.

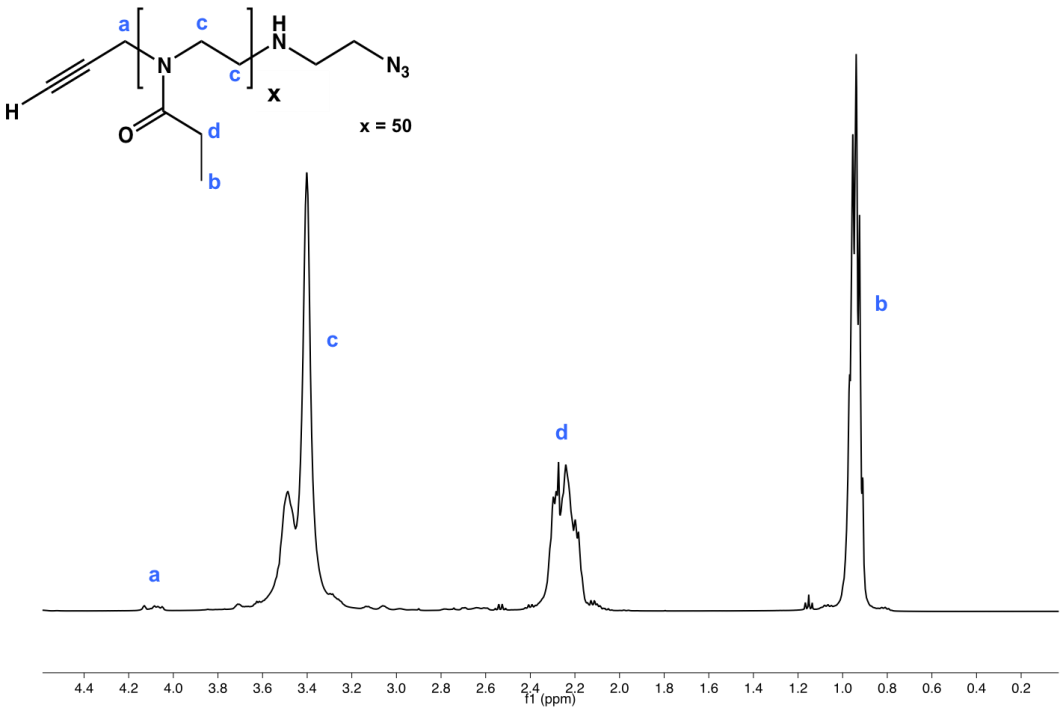

Figure S9. ^{1}H-NMR spectrum (500 MHz) of propargyl-l-PEOXA-azide in D_2O.

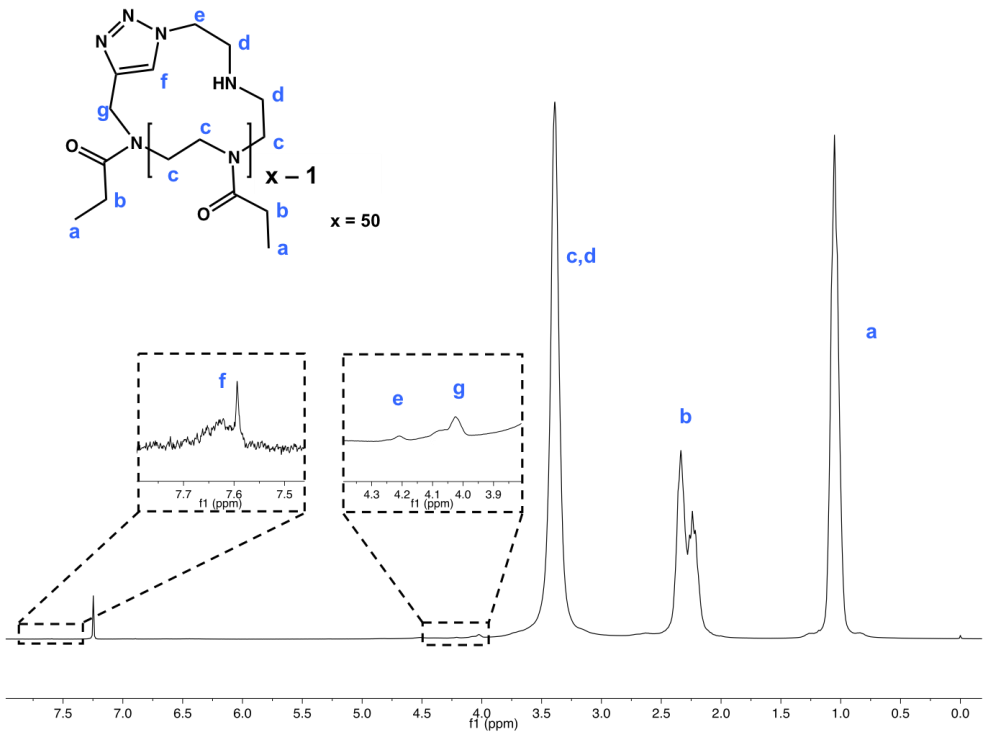

Figure S10. ^{1}H-NMR spectrum (500 MHz) of c-PEOXA in $CDCl_3$.

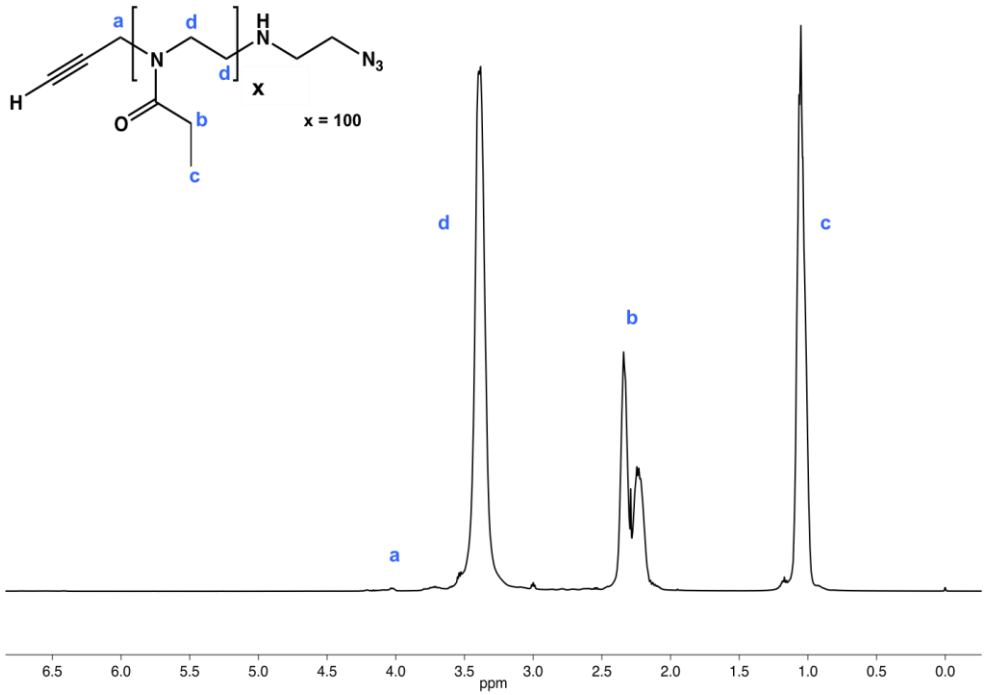

Figure S11. ^{1}H-NMR spectrum (500 MHz) of propargyl-L-PEOXA-azide in $CDCl_3$.

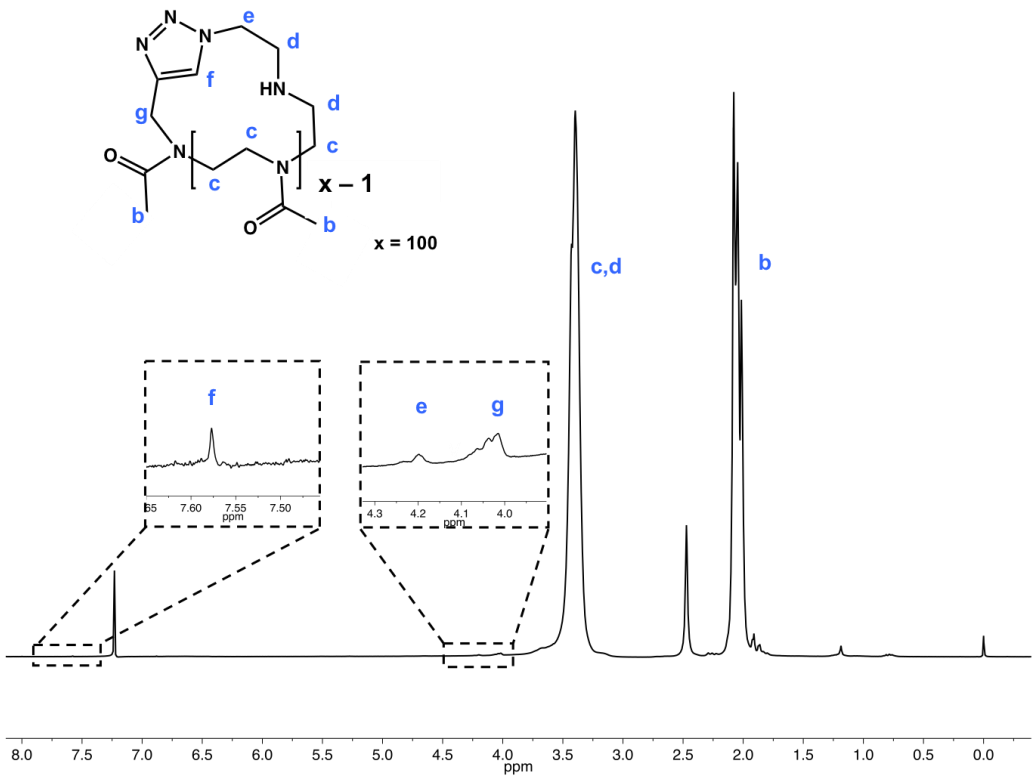

Figure S12. ^{1}H-NMR spectrum (500 MHz) of C-PEOXA in $CDCl_3$.

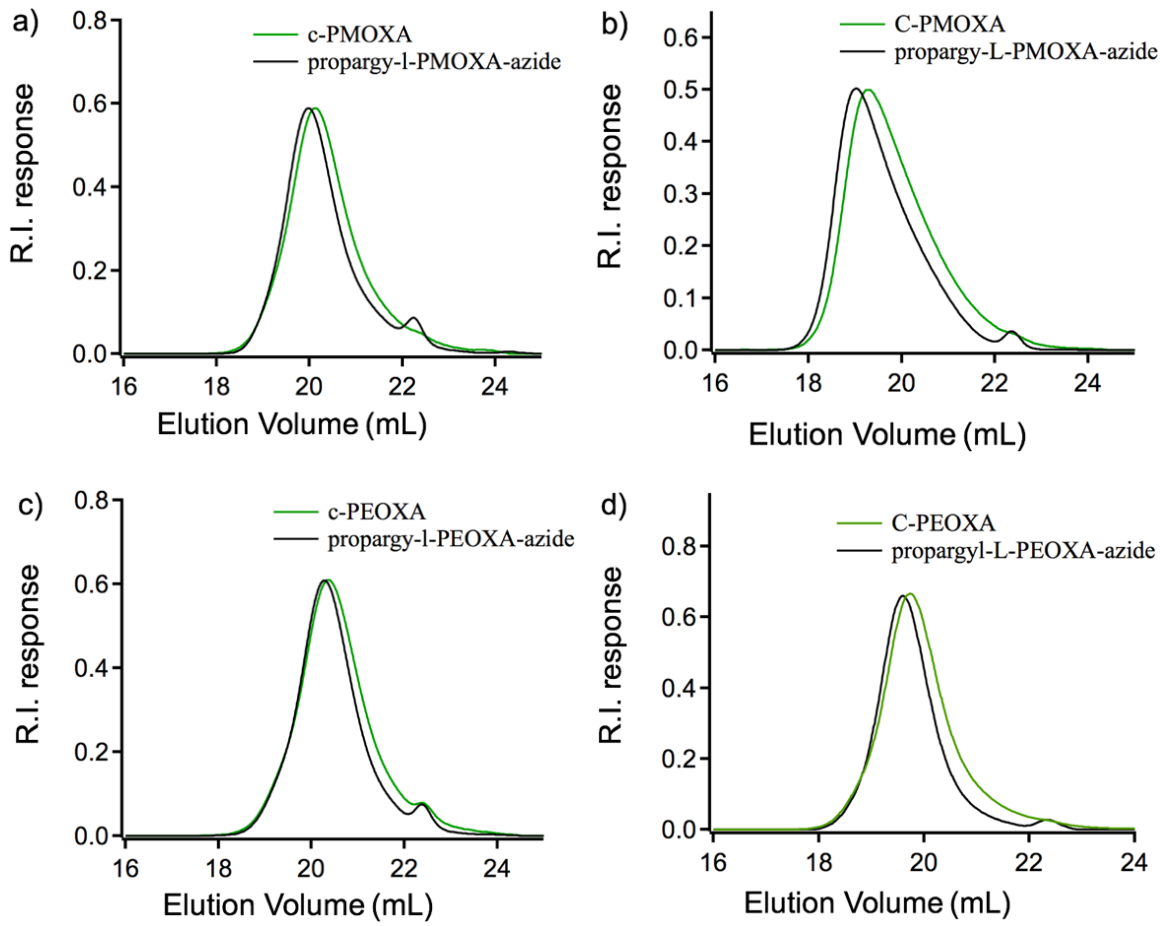

Figure S13. GPC elution curves of cyclic PMOXA and their precursors (a,b) and of cyclic PEOXA and their precursors (c,d). The shift towards higher elution times for the cyclic PAOXA indicates the successful cyclization.

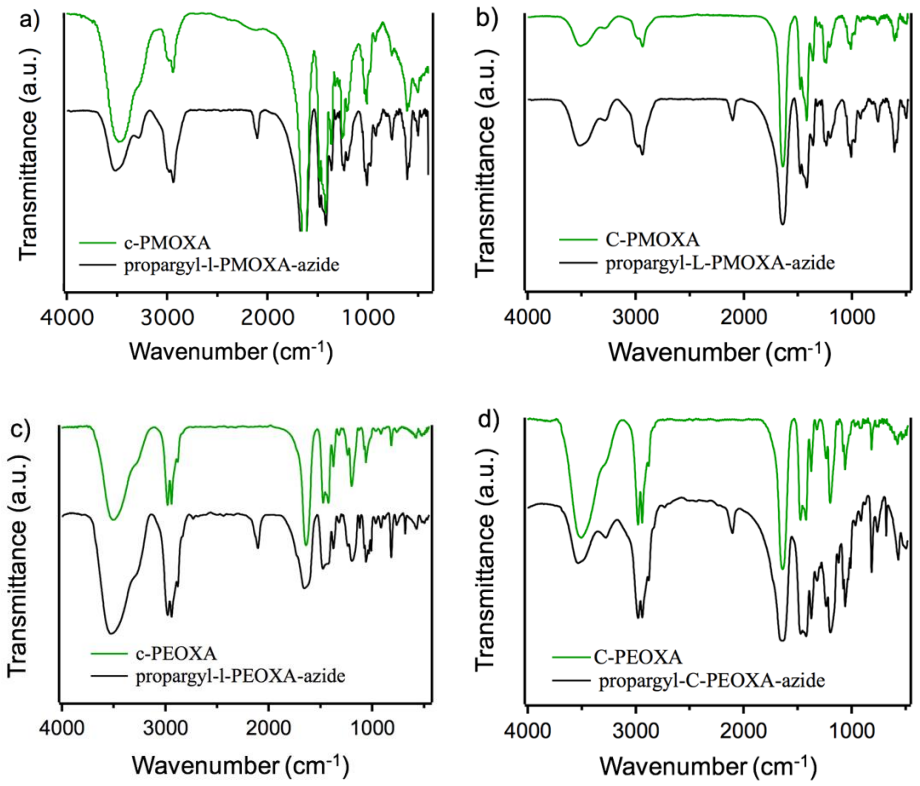

Figure S14. FT-IR spectra of cyclic PMOXA and their precursors (a, b) and of cyclic PEOXA and their precursors (c, d). The disappearance of the azide signal at 2100 cm^{-1} for the cyclic PAOXA confirms the ring closure.

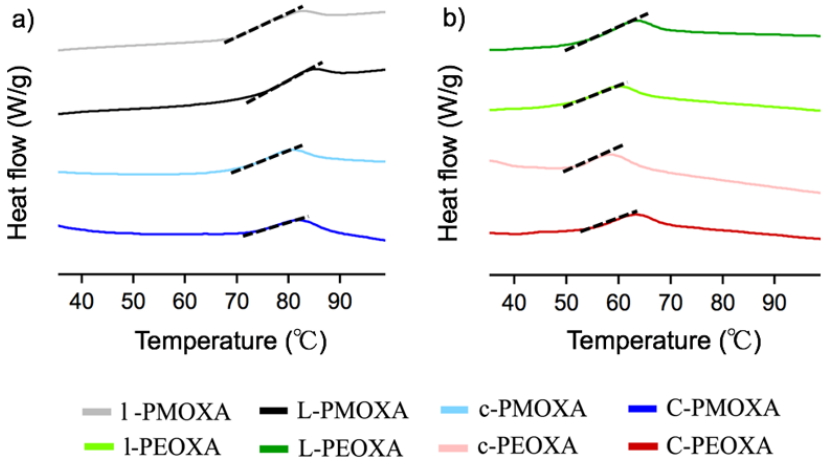

Figure S15. DSC curves of topologically different PMOXA (a) and PEOXA (b). The glass transition regions are indicated by the dashed lines.

Table S1. Glass transition temperatures (Tg) of topologically different PAOXA, calculated from DSC.

Type of PAOXA	T_g (°C)	Type of PAOXA	T_g (°C)
l-PMOXA	75	l-PEOXA	56
L-PMOXA	79	L-PEOXA	58
c-PMOXA	75	c-PEOXA	55
C-PMOXA	78	C-PEOXA	60

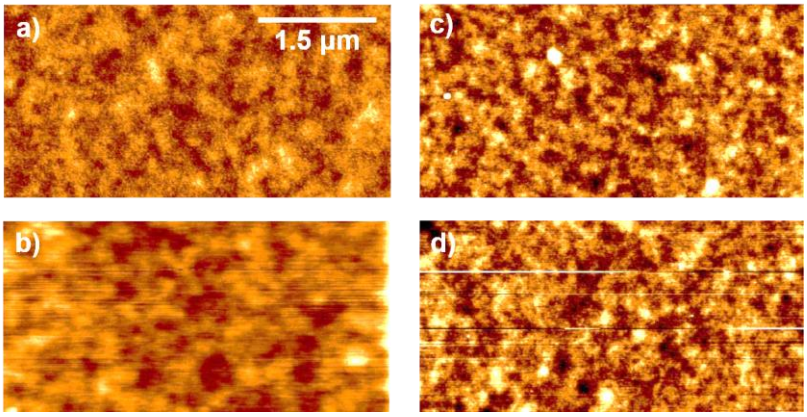

Figure S16. AFM tapping mode height micrographs of PGMA brushes synthesized by SI-ATRP. (a) PGMA brushes in air; (b) PGMA brushes immersed in ultra-pure water; (c) PGMA brushes analysed in air after overnight treatment at 150°; (d) PGMA brushes analysed in ultra-pure water after overnight treatment at 150°. RMS values recorded on a 2,5 x 2,5 μm^2 are 0.45 ± 0.06 nm (a), 0.51 ± 0.1 nm (b), 0.70 ± 0.08 nm (c) and 0.73 ± 0.11 nm (d).

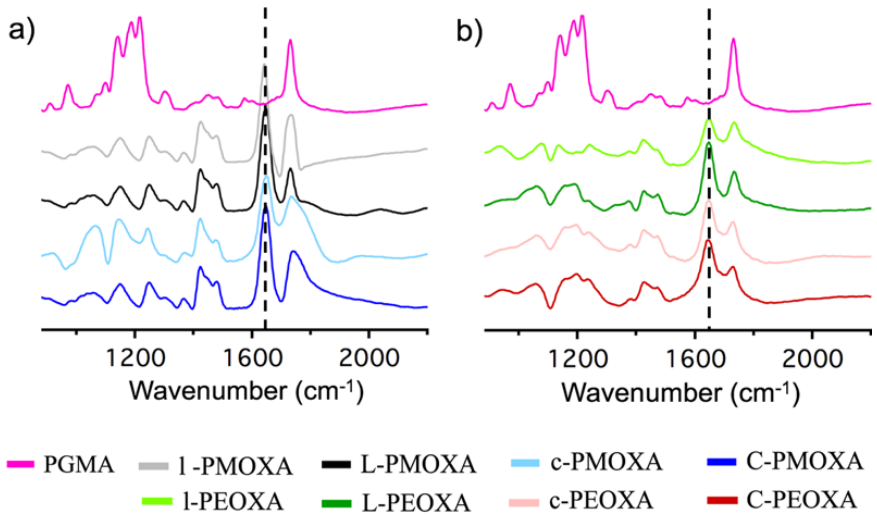

Figure S17. MTR-IR spectra of PGMA, PGMA/PMOXA (a) and PGMA/PEOXA (b) films. The spectra of PGMA and PGMA/PAOXA films showed the signal related to the stretching of the methacrylate ester bond at 1732 cm^{-1}. After thermal treatment the signal related to the amide stretching of PAOXAs appeared at 1639 cm^{-1}, suggesting their successful grafting, while the bands correlated to the epoxy groups of PGMA, between 1300 and 900 cm^{-1}, disappeared, confirming the crosslinking of the brush underlayer.

X-ray photoelectron spectroscopy (XPS)

XPS was performed using a Sigma Probe (Thermo Fisher Scientific, East Grinstead, UK) spectrometer. The spectra were recorded using a monochromatic Al Kα source (power of 200 W).

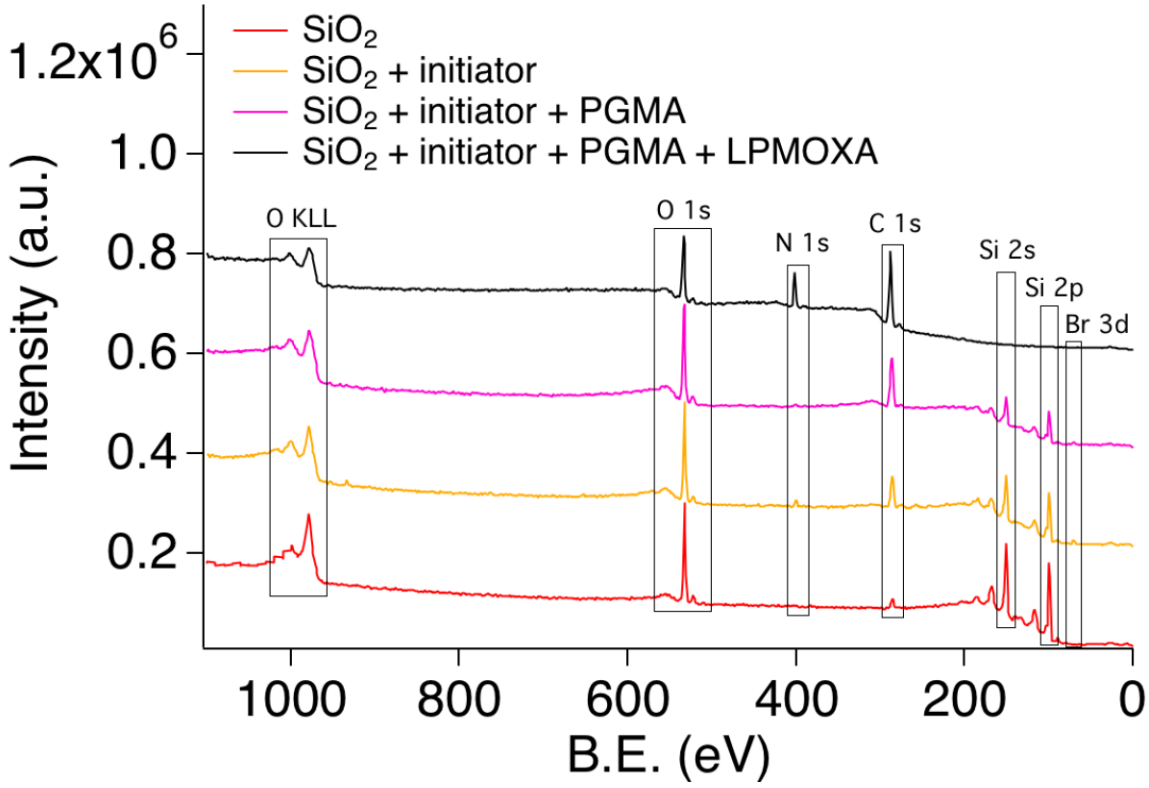

Figure S18. XPS survey spectra recorded on PGMA/LPMOXA bilayer brushes after each functionalization step. The spectrum from the initiator-bearing self-assembled monolayer (SAM) showed the Br 3d signal and the N 1s peak from the APTES-based anchor. Following grafting of PGMA brushes by SI-ATRP, the intensity of the N 1s peak was reduced, while the C 1s signal originating from the PGMA backbones became stronger. Final thermal grafting of LPMOXA was corroborated by the disappearance of the Si 2s, confirming the uniform screening of the underlying substrate, the appearance of a strong N 1s signal from the oxazoline repeating units, and a further strengthening of the C 1s.

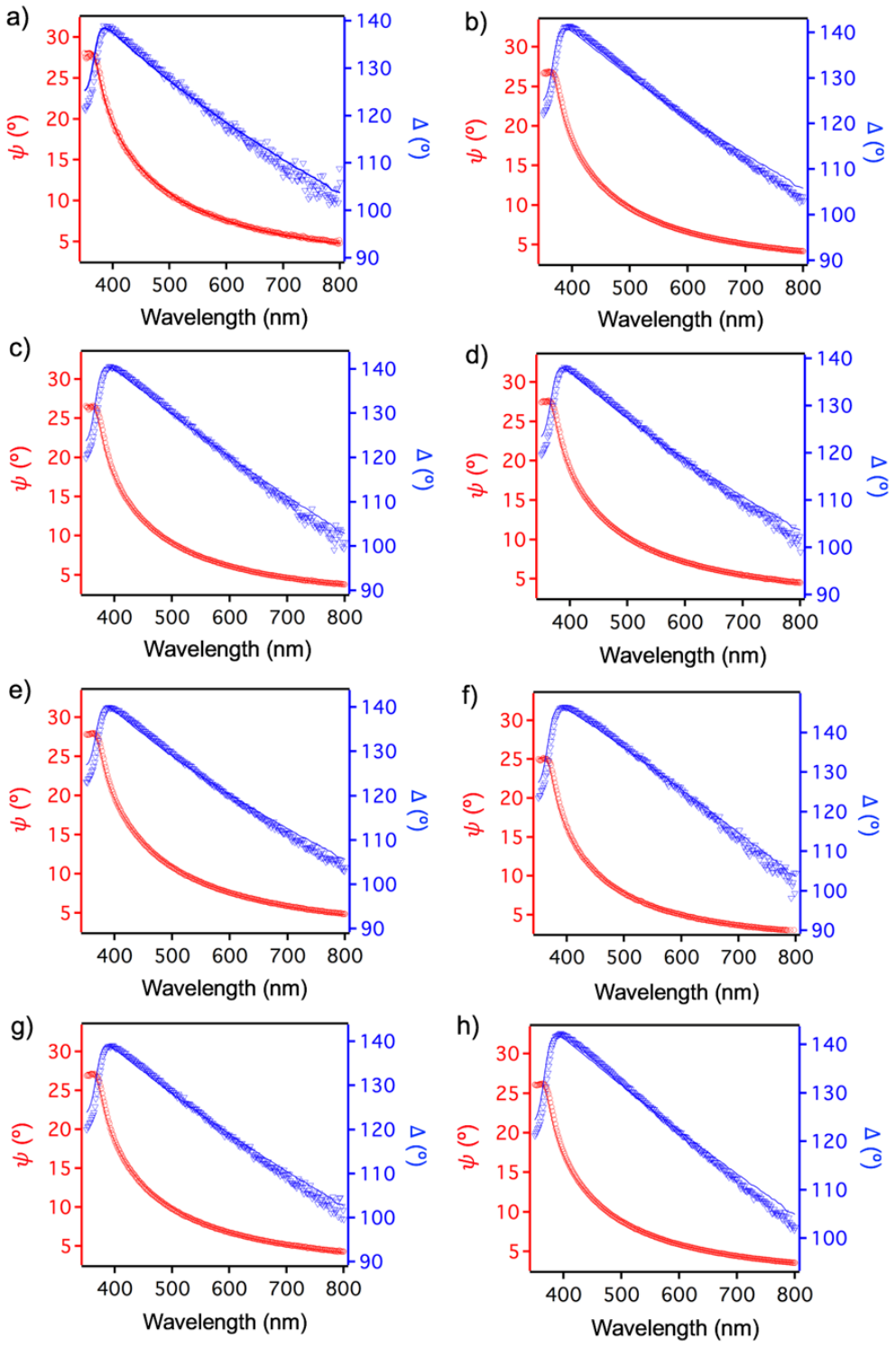

Figure S19. VASE data showing Ψ (red) and Δ (blue) as a function of wavelength (350-800 nm). The data points represent experimental results, while the solid lines are simulated spectra. PGMA/PAOXA bilayered films: a) l- PMOXA, b) L-PMOXA, c) c-PMOXA, d) C-PMOXA, e) l-PEOXA, f) L-PEOXA, g) c-PEOXA, h) C-PEOXA.

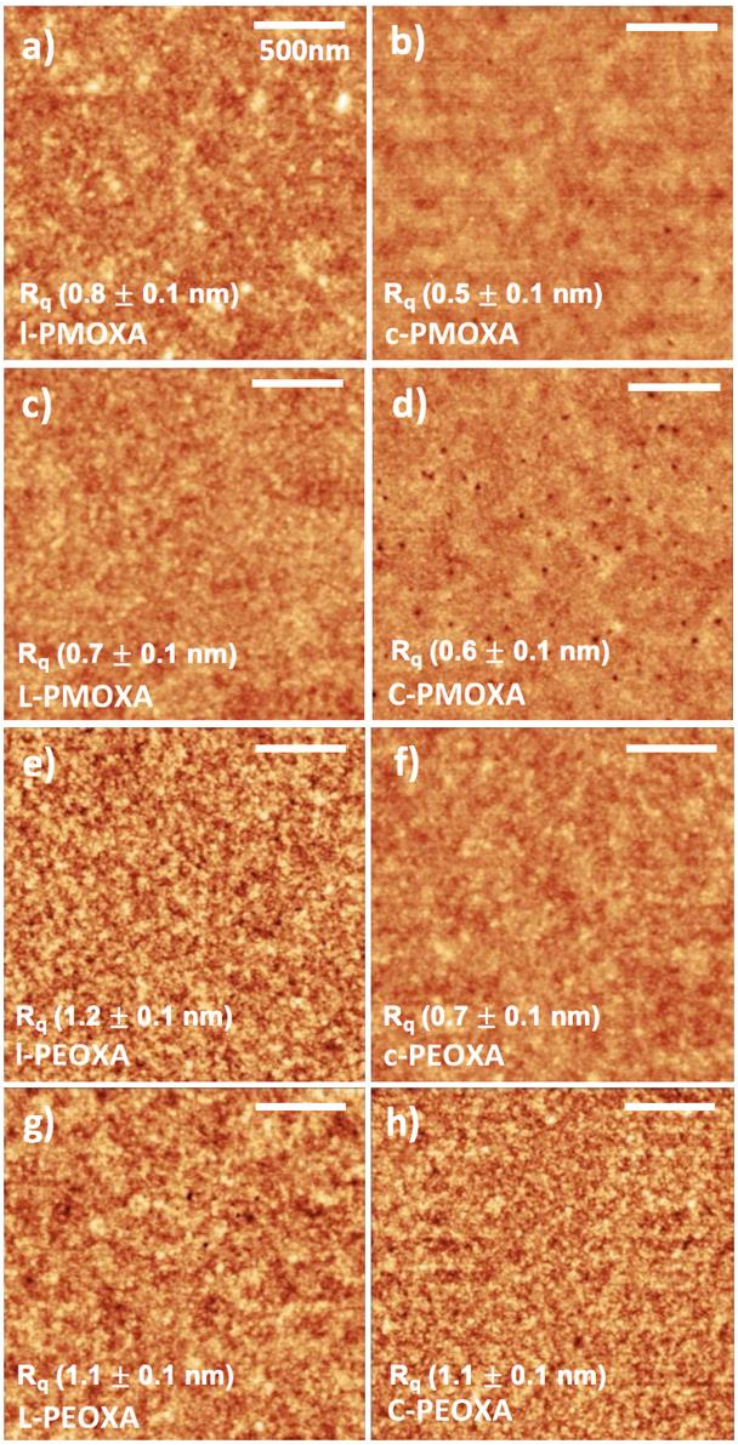

Figure S20. AFM micrographs of PGMA/PMOXA and PEOXA bilayered films. RMS roughness values for each image were calculated and listed as R_q.

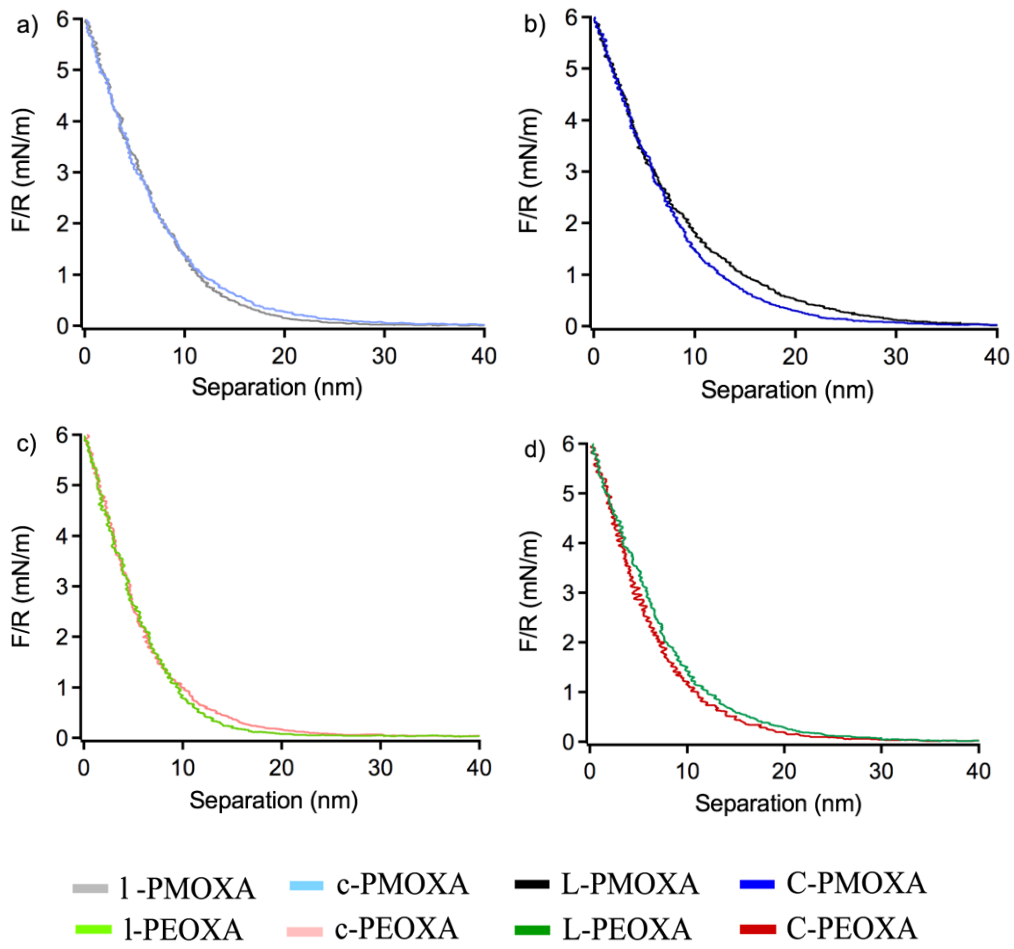

Figure S21. Approaching force vs separation (F-S) profiles recorded in PBS on PGMA/PMOXA (a,b) and PGMA/PEOXA (c,d) bilayered films presenting different topology. Each F-S curve was collected at a speed of 2 μm s^{-1} using a 10 μm radius silica colloidal probe cantilever with normal spring constant of 0.21 N m^{-1}.

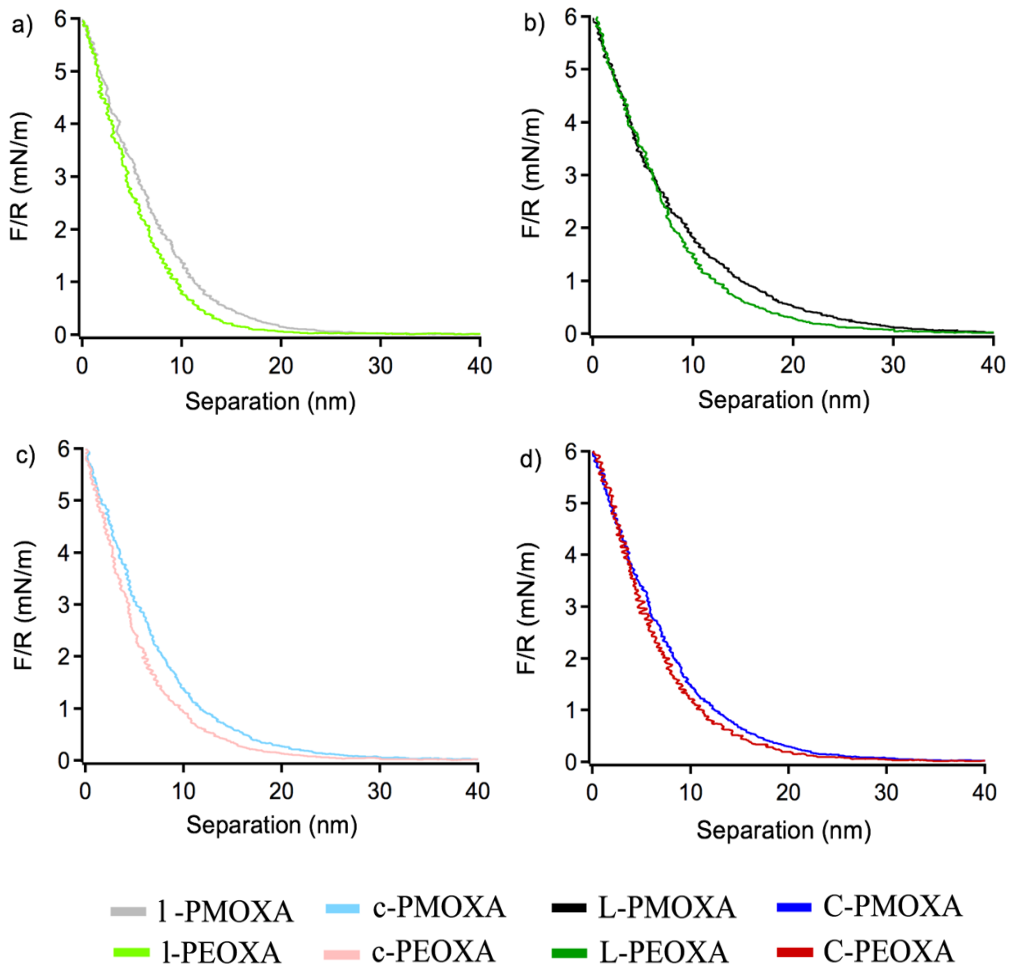

Figure S22. Approaching force vs separation profiles recorded in PBS on PGMA/linear PMOXA and PEOXA (a,b) and PGMA/cyclic PMOXA and PEOXA (c,d) bilayered films presenting different side groups. Each F-S curve was collected at a speed of 2 μm s^{-1} using a 10 μm radius silica colloidal probe cantilever with normal spring constant of 0.21 N m^{-1}.

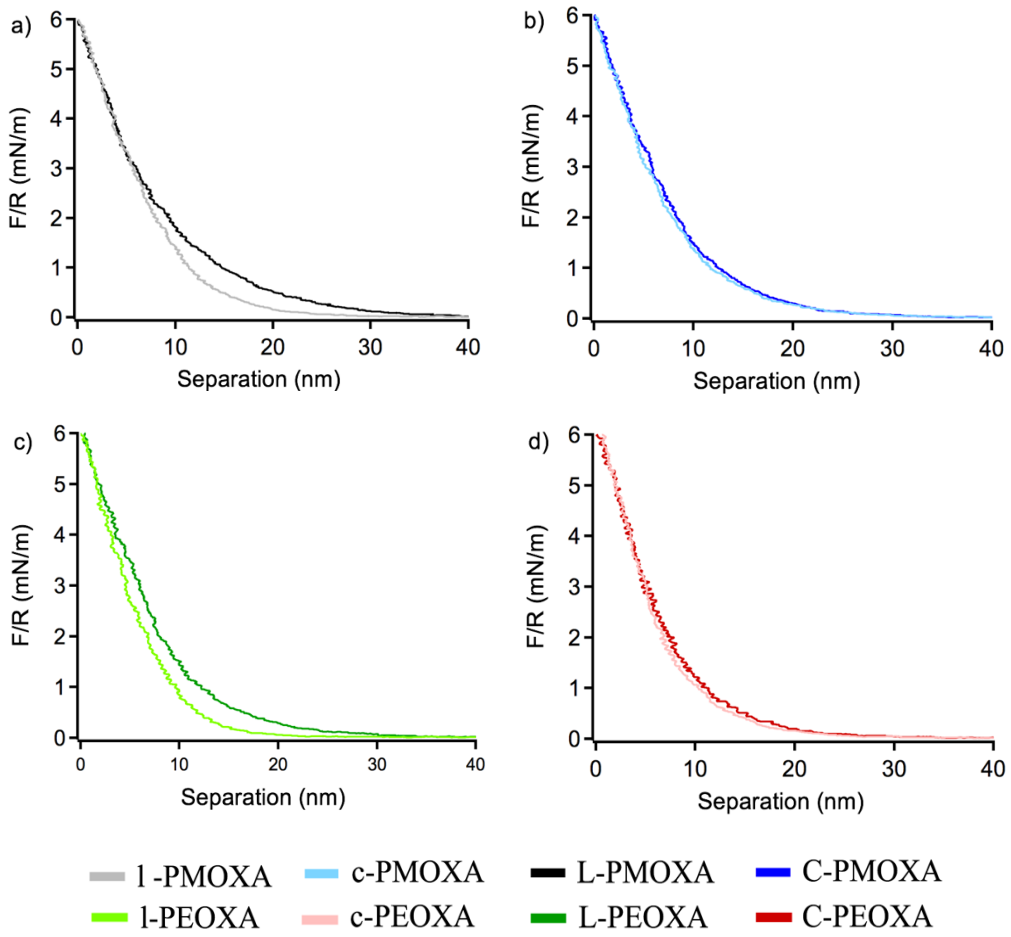

Figure S23. Approaching force vs separation profiles recorded in PBS on PGMA/PMOXA (a,b) and PGMA/PEOXA (c,d) bilayered films presenting different chain length. Each F-S curve was collected at a speed of 2 μm s^{-1} using a 10 μm radius silica colloidal probe cantilever with normal spring constant of 0.21 N m^{-1}.

Table S2. Coefficient of friction of PGMA/PMOXA and PEOXA bilayered films calculated from friction force vs applied load curves reported in Figure 3 of the manuscript.

Type of interfacial grafts	μ	Type of interfacial grafts	μ
l-PMOXA	0.13	l-PEOXA	0.67
L-PMOXA	0.06	L-PEOXA	0.42
c-PMOXA	0.05	c-PEOXA	0.47
C-PMOXA	0.05	C-PEOXA	0.34

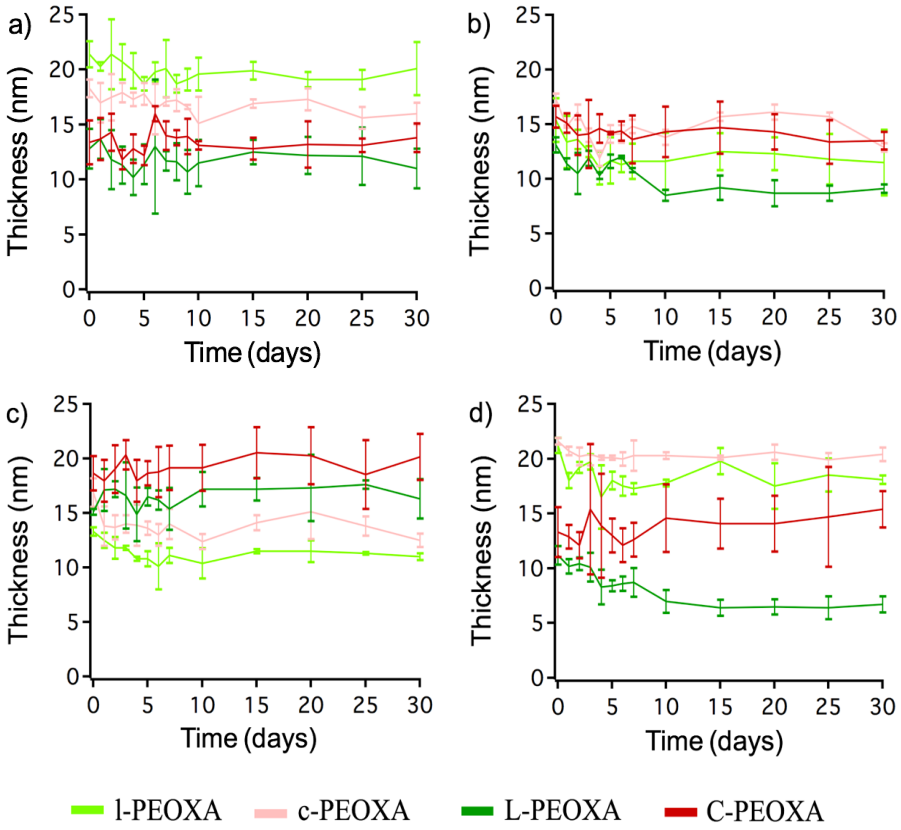

Figure S24. Long-term stability of the PGMA/PEOXA bilayered films presenting different topology. Film thicknesses were measured by VASE over time, after incubation in ultra-pure water a) in PBS b) in tap water c) and in water from Lake Zürich d).

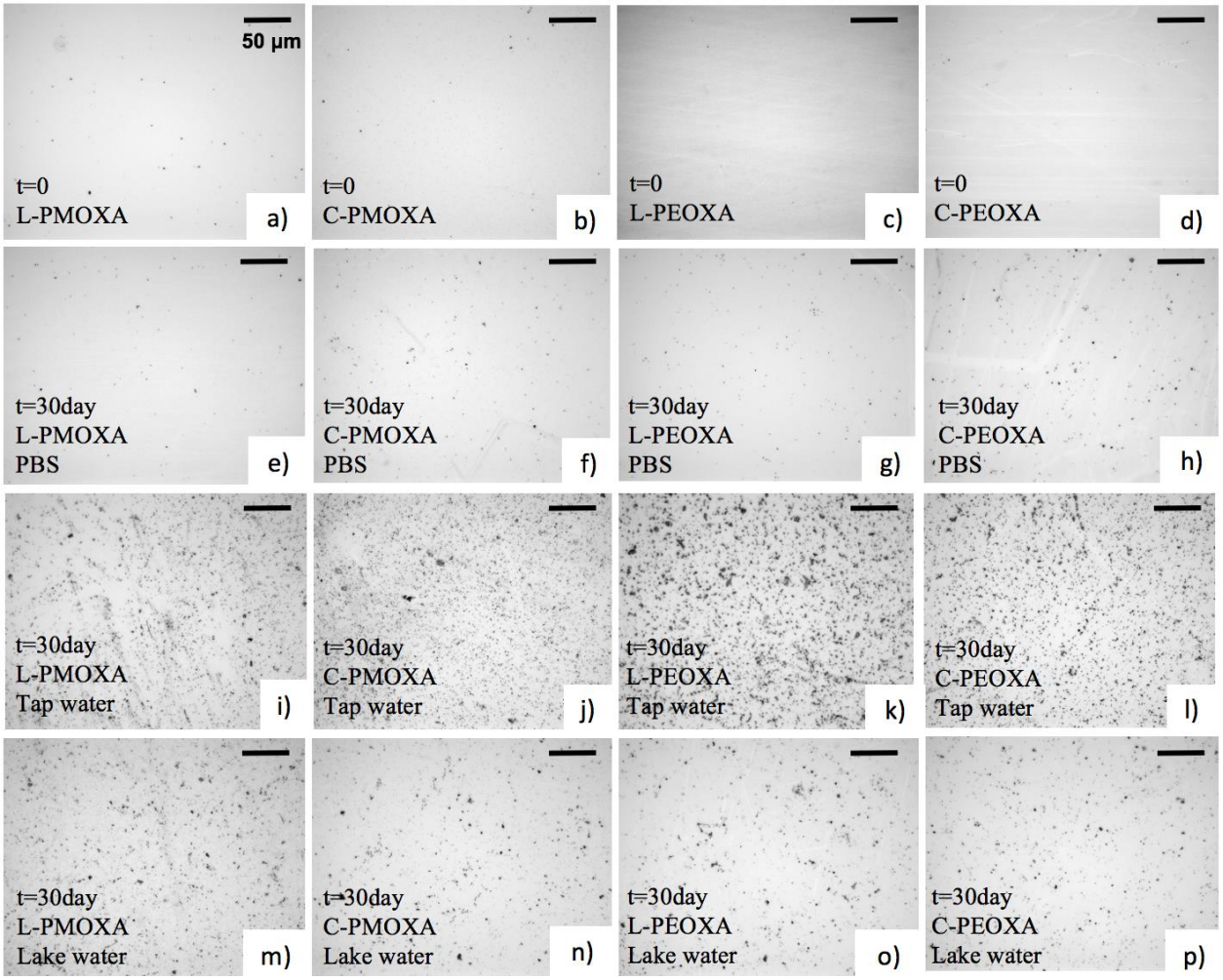

Figure S25. Optical microscopy images of PGMA/PMOXA and PEOXA bilayered films, recorded before (a-d) and after exposure to PBS (e-h), to tap water (i-l) and to water from Lake Zürich (m-p).

Comparison between PGMA/LPMOXA-NH_2, PGMA/LPMOXA-NH-propyl and PGMA/propargyl-PMOXA-N_3

In order to confirm that linear PAOXA adsorbates (presenting a primary amino group as anchor) and cyclic analogues (presenting a secondary amino function) featured the same reactivity towards PGMA brush films, we synthesized L-PMOXA adsorbates terminating with amino-propyl group (shown in Figure S26 below) and compared the structural and interfacial properties of the generated PGMA/L-PMOXA-aminopropyl bilayer films with those displayed by PGMA/L-PMOXA-NH_2 and PGMA/propargyl-PMOXA-azide (precursor of the cyclic PMOXA) by a combination of VASE and AFM.

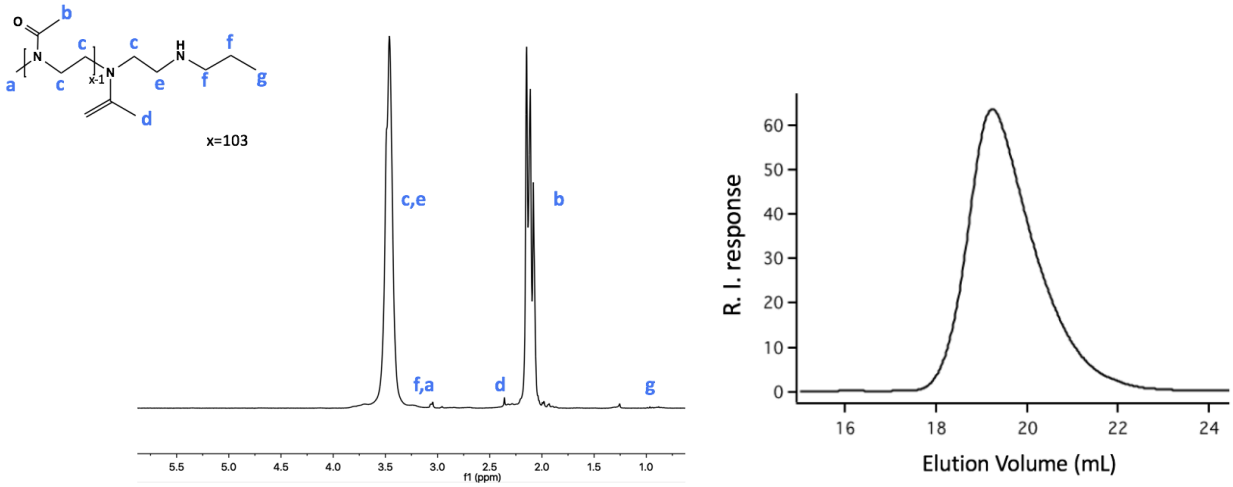

Figure S26. HNMR spectrum and GPC elugram of L-PMOXA-NHpropyl.

Table S3. Structural properties of PGMA/L-PMOXA bilayer films

PAOXA adsorbate	M_n (DP)	Đ	T_{PGMA} [nm]	$T_{PGMA-PAOXA}$ [nm]	TR	σ [chains nm^{-2}]
L-PMOXA-NH_2	7600 (89)	1.3	5.2 ± 0.3	17.4 ± 1.2	2.4	1.3 ± 0.1
L-PMOXA-NHpropyl	8800 (103)	1.2	5.4 ± 0.4	19.5 ± 2.6	2.6	1.1 ± 0.2
propargyl-PMOXA-N_3	8100 (95)	1.3	5.0 ± 0.7	18.6 ± 5.4	2.7	1.1 ± 0.1

As can be seen in Table S3, the grafting efficiency for L-PMOXA-NH_2, L-PMOXA-NHpropyl and propargyl-PMOXA-N_3 on PGMA brushes was very similar, as confirmed by the comparable values of bilayer brush thickness ($T_{PGMA-PAOXA}$), increased thickness (defined as «thickening ratio», TR) and final PAOXA grafting density (σ).

Interfacial brushes presenting comparable density and structure thus indicated a similar reactivity by the PMOXA adsorbates.

We subsequently tested the stiffness of the different bilayer PGMA/PMOXA brushes and their nanotribological properties by colloidal probe AFM and LFM, respectively, in order to confirm that crosslinking of PGMA was solely determined by the thermal treatment and that only the interfacial composition of PAOXA brushes governed the recorded friction.

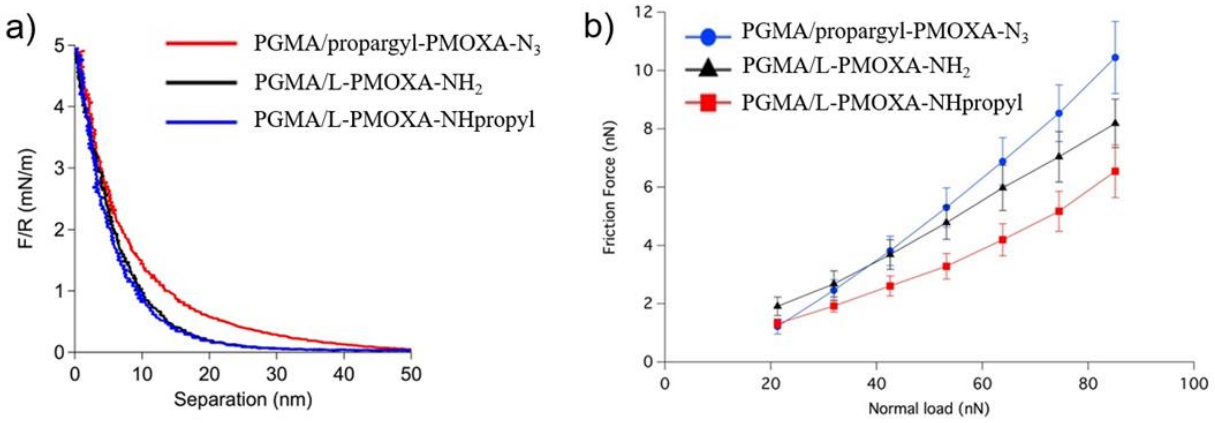

Figure S27. FS (a) and FfL profiles (b) recorde by AFM and LFM, respectively, on the different PGMA/L-PMOXA bilayer brushes.

As can be seen in the force vs separation (FS) profiles reported in Figure S27a, the nanomechanical properties of PGMA/L-PMOXA-NH_2 and PGMA/L-PMOXA-NHpropyl bilayer brushes were comparable. In contrast, the interaction between PGMA/propargyl-PMOXA-N_3 and the AFM probe was determined by the different interfacial composition of the PMOXA brush, which exposed propargyl-terminating chains at the interface. In a similar way, friction vs applied load profiles (FfL) recorded on PGMA/L-PMOXA-NH_2 and PGMA/L-PMOXA-NHpropyl bilayer brushes nearly overlapped each other, both these brushes exposing PMOXA grafts with similar densities at the

interface, while a lower friction was recorded on PGMA/propargyl-PMOXA-N_3 films, presumably due to the different groups exposed at the interface.